Quantifying the impacts of modeling uncertainties on the seismic drift demands and collapse risk of buildings with implications on seismic design checks

Beliz U. Gokkaya*,†, Jack W. Baker and Greg G. Deierlein

Department of Civil & Environmental Engineering, John A. Blume Earthquake Engineering Center, Stanford University, Stanford, CA 94305, USA

SUMMARY

Robust estimation of collapse risk should consider the uncertainty in modeling of structures as well as variability in earthquake ground motions. In this paper, we illustrate incorporation of the uncertainty in structural model parameters in nonlinear dynamic analyses to probabilistically assess story drifts and collapse risk of buildings. Monte Carlo simulations with Latin hypercube sampling are performed on ductile and non-ductile reinforced concrete building archetypes to quantify the influence of modeling uncertainties and how it is affected by the ductility and collapse modes of the structures. Inclusion of modeling uncertainty is shown to increase the mean annual frequency of collapse by approximately 1.8 times, as compared with analyses neglecting modeling uncertainty, for a high-seismic site. Modeling uncertainty has a smaller effect on drift demands at levels usually considered in building codes; for the same buildings, modeling uncertainty increases the mean annual frequency of exceeding story drift ratios of 0.03 by 1.2 times. A novel method is introduced to relate drift demands at maximum considered earthquake intensities to collapse safety through a joint distribution of deformation demand and capacity. This framework enables linking seismic performance goals specified in building codes to drift limits and other acceptance criteria. The distributions of drift demand at maximum considered earthquake and capacity of selected archetype structures enable comparisons with the proposed seismic criteria for the next edition (2016) of ASCE 7. Subject to the scope of our study, the proposed drift limits are found to be unconservative, relative to the target collapse safety in ASCE 7. Copyright © 2016 John Wiley & Sons, Ltd.

1. INTRODUCTION

Owing to the variability in earthquake ground motions and the uncertainty in structural model idealizations, any efforts to rigorously assess collapse safety should consider these effects. For collapse assessment by nonlinear dynamic analysis, this includes reliable characterization and propagation of the aforementioned sources of uncertainty through the analysis. Ground motion variability and its impacts on seismic response assessment has been studied by many researchers who have proposed ground motion selection and analysis strategies for taking into account record-to-record variability [e.g., 1, 2, and others]. Another important contributor to the robustness of seismic response predictions is modeling uncertainty [3]. A blind prediction contest to analyze the response of a single bridge

---

*Correspondence to: Beliz U. Gokkaya, Department of Civil & Environmental Engineering, John A. Blume Earthquake Engineering Center, Stanford University, Stanford, CA 94305.
†E-mail: beliz@alumni.stanford.edu

column [4] highlighted the significance of modeling uncertainty in structural seismic response predictions. The variability in the engineering parameters submitted by the contestants were remarkable for this highly constrained experiment. Maximum displacements were predicted under different earthquake ground motions with an average coefficient of variation of 0.4 and the median bias of the predictions corresponding to different ground motions ranged from 5% to 35%.

Probabilistic approaches has been proposed for uncertainty analysis in seismic design and assessment of structures [e.g., 5, 6, and others] . Seismic fragility curves [7, 8] are commonly used for assessment of performance goals in structures. One of the major challenges in incorporating modeling uncertainty into seismic response assessment is balancing computational demand and accuracy. Sensitivity analysis provides insight regarding relative importance of modeling parameters [9–11], and first-order second-moment is often used to propagate modeling uncertainty in seismic performance assessment [e.g., 12,13] However, first-order second-moment can loose accuracy when the relationship between input and response variables is nonlinear, which is a concern when modeling collapse. Methods such as nonlinear response surface [14] and artificial neural network methods have been used to incorporate nonlinearities, although most of these methods do not scale efficiently or accurately when the number of random variables increase. Among the available methods, Monte-Carlo based methods remain as the most flexible and scalable methods to account for modeling uncertainty, albeit sometimes at large computational expense [e.g., [15–17]].

In this paper, Monte-Carlo based simulations are used to incorporate the variability of structural model parameters in nonlinear dynamic analyses for assessing deformations and collapse risk of buildings under earthquake ground motions. A set of archetype buildings are analyzed to quantify the significance of modeling uncertainty and to examine its implication on design approaches that utilize nonlinear dynamic analysis. The effects of modeling uncertainty are evaluated for both ductile and non-ductile reinforced concrete structures to investigate whether the extent to which ductility and strength irregularities influence the significance of modeling uncertainties. The procedures illustrate and contrast so-called multiple stripe analyses (MSA) versus incremental dynamic analyses (IDA) for ground motion selection and scaling, each of which has its advantages and limitations. MSA conducted with hazard consistent ground motions are used to directly evaluate collapse resistance in terms of spectral ground motion intensity, whereas IDA are used to establish drift capacities of the buildings, which can then be used together with drift demands to assess collapse safety. In addition to outlining consistent procedures for evaluating modeling uncertainties for collapse risk, results of the study provide benchmark data to help establish guidelines to account for modeling uncertainties in design and assessment.

The approach to evaluating collapse risk through drift demands is motivated in part by emerging methods to validate building designs using nonlinear dynamic analysis. For example, guidelines for the seismic design of tall buildings [18, 19] and a recently proposed update for the next edition of ASCE 7 [20] rely heavily on story drift limits, determined from nonlinear dynamic analyses, to help ensure that buildings meet minimum collapse safety targets. To investigate collapse drift capacities and their relationship to calculated drift demands, a probabilistic framework is proposed to jointly quantify joint drift demands and capacities, including uncertainties associated with both ground motions and structural modeling parameters. This framework is employed in nonlinear analyses to characterize the joint distribution of peak drift at maximum considered earthquake level and capacity for selected archetype structures. The resulting distributions are used to assess the proposed acceptance criteria for new provisions in ASCE 7 [20] and provide a strategy for improved calibration of such acceptance criteria.

2. SEISMIC PERFORMANCE ASSESSMENT

A risk-based seismic assessment strategy is adopted for using nonlinear dynamic analyses to assess the impacts of both ground motion and modeling uncertainty on drift demands and collapse. Illustrated in Figure 1 are key aspects of the assessment procedure. Referring to Figure 1(a), a so-called MSA approach is used, wherein nonlinear dynamic analyses are conducted using suites of ground motions that are selected and scaled to match the unique seismic hazard at a building site. MSA involves conducting nonlinear time history analyses at multiple levels of ground motion intensity, where at each
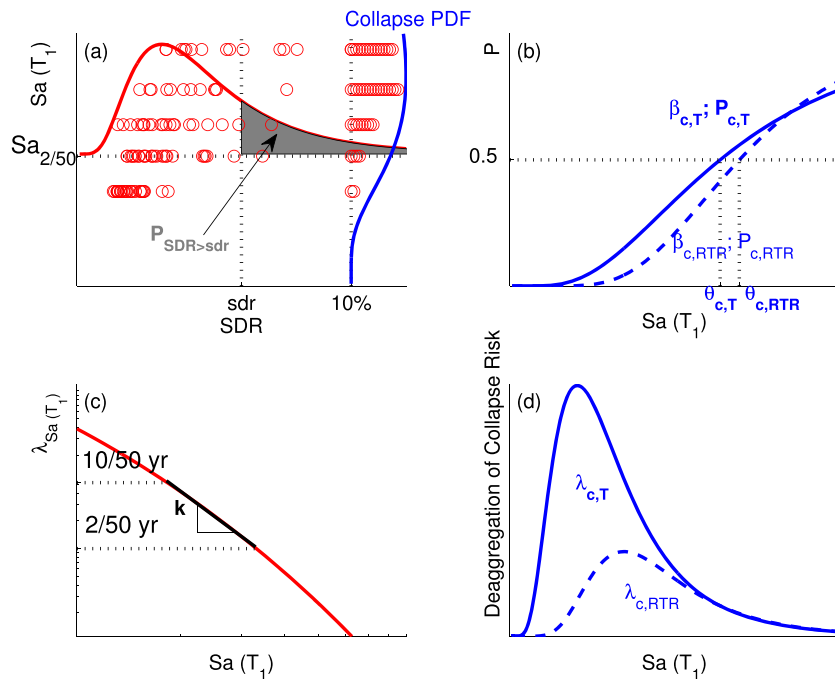
Figure 1. Illustration of seismic performance assessment (a) Multiple stripes analyses at different ground motion intensity levels (b) Collapse and drift-exceedance fragility functions (c) Seismic hazard curve (d) Collapse risk deaggregation curves. SDR, story drift ratio.

intensity, the distribution of peak story drift ratio (SDR) and other engineering demand parameters of interest are recorded. In this study, the ground motions are selected and scaled using a conditional spectra approach, where the ground motion intensity is defined based on the spectral acceleration at the fundamental period of structure, $Sa(T_1)$, and the conditional spectra characterizes the target response spectra, including mean and variability, that are derived from probabilistic seismic hazard analysis [21]. Hazard consistent ground motions are selected at different intensity levels, ideally from the onset of significant inelasticity up to about the intensity where about half of the ground motions cause collapse. For the code-conforming buildings considered in this study, the ground motions are evaluated at five intensities with frequencies of exceedance ranging from 5% in 50 years to 1% in 200 years.

In Figure 1(a), the points at each intensity stripe provide data to characterize the maximum story drift demands and the frequency of collapse. Because the exact onset of collapse is not detected in the typical MSA procedure, a SDR in excess of 10% is used as indicator of structural collapse because at this level most engineering structures are identified to have no or insufficient stiffness [22]. Thus, the incidences of collapse at each intensity can be used to compile vertical statistics to fit a lognormal distribution of collapse probability, in terms of $Sa(T_1)$. This distribution is illustrated by the collapse probability density function (PDF) in Figure 1(a) and the corresponding collapse cumulative distribution function (CDF) in Figure 1(b). Data at each ground motion intensity stripe are used to determine horizontal statistics of drift exceedance probability distributions, shown by the drift PDF in Figure 1(a). Integrating regions of the drift PDF at each intensity level, such as the $P(SDR > sdr)$ shown in Figure 1(a), can then be used to develop drift exceedence CDF's. As described later in Sections 5 and 6, horizontal statistics of the drift data become relevant when evaluating drift demands at specified ground motion intensities. Also discussed in Section 5 are the impacts of modeling uncertainty on drift exceedence CDF's, which defines $P(SDR > sdr)$, for alternating values of sdr.

Collapse fragility curves obtained using MSA data are shown by the blue lines in Figure 1(b), where two estimates of collapse fragility curves are provided. One estimate, shown by the dashed line, is obtained by analyses using median model parameters. As such, this estimate incorporates only record-to-record variability (RTR) in the ground motions and, hence, carries the subscript RTR. The second

estimate, shown in the solid line, is from analyses that incorporate both record-to-record variability as well as modeling uncertainty and carries the subscript T, indicating it includes a total estimate of uncertainty. Collapse limit state is indicated with subscript c.

The collapse fragility curves in Figure 1(b) are represented by lognormal distributions, which are described by a logarithmic mean ($ln(\theta)$ where θ is the median) and logarithmic standard deviation (also known as dispersion, β). All parameters of interest are used with appropriate subscripts, wherever applicable, corresponding to their limit states and the type of uncertainty they include, that is, $\theta_{c,T}$ versus $\theta_{c,RTR}$.

Risk-based assessment of structural response provides the mean annual frequency of exceedance (λ) of certain limit performance states (collapse or drift exceedence) given the seismic hazard at the design site of the structure. Figure 1(c) illustrates a seismic hazard curve. The λ for each limit state can be obtained by integrating the corresponding fragility curve with the seismic hazard curve. The λ_c defining the mean annual frequency of collapse is obtained as follows:

$$\lambda_c = \int_0^\infty P(C|IM = im) \left| \frac{d\lambda_{IM}(im)}{d(im)} \right| d(im) \tag{1}$$

where $P(C|IM = im)$ defines the probability of collapse given the ground motion intensity $IM = im$, and $\left| \frac{d\lambda_{IM}(im)}{d(im)} \right|$ defines the absolute value of the slope of the hazard curve at im.

Deaggregation of λ_c helps identify the ground motion intensities that contribute most in estimating λ_c [23]. These curves plot the integrand of Equation (1) with respect to IM. Deaggregation curves of λ_c with and without modeling uncertainty are provided in Figure 1(d), where the areas under these curves yield λ_c.

We see from Figure 1(b) that, in the presence of modeling uncertainty, the collapse fragility curve has smaller median collapse capacity and higher dispersion. This results in ground motions having smaller intensities and higher rates of occurrence contributing more to λ_c as shown in Figure 1(d).

In the following sections, we use the aforementioned seismic performance assessment strategy along with the presented performance metrics to quantify the impacts of modeling uncertainty for an extensive set of archetype structures.

3. CASE STUDY SEISMIC RESPONSE ANALYSIS WITH MODELING UNCERTAINTY

3.1. Structural models

Thirty ductile reinforced concrete frame buildings were designed by [13] using modern building code standards [24, 25] for a high-seismicity site at Los Angeles (LA), California. These buildings range in height from 1 to 20 stories, including a few designs that have varying amounts of strength irregularity up the building height. The structural systems are analyzed using Open System for Earthquake Engineering Simulation Platform [26] using concentrated plasticity models. An illustrative structural idealization is provided in Figure 2(a) and the detail of the beam-column connections is provided corresponding to ductile frames. Frame elements are modeled as elastic members having rotational springs at the ends, whose hysteretic behavior is governed by a trilinear backbone curve (Figure 2(b)) and cyclic and in-cycle degradation rules [27]. The parameters defining the M-θ hinge model are determined using empirical equations that are calibrated using a dataset consisting of experimental test results of over two hundred reinforced concrete columns [28].

Three non-ductile reinforced concrete frame buildings of 2, 4, and 8 stories in height were designed by [29] according to the 1967 Uniform Building Code [30] for a high-seismicity site at Los Angeles, CA, USA. Similar to the ductile frames, the flexural response of beams and columns are modeled using the concentrated plasticity model as in Figure 2(b), but with less ductile properties. In addition, the column models include zero-length shear and axial springs (Figure 2(c)) to idealize shear and axial failure, respectively. Axial springs have limit surfaces defined by the force-displacement relationship given by [31]. Shear springs have limit strengths defined by [32] in the small displacement range, which is triggered in the case of a brittle shear failure, and they have a deformation limits defined by [31]
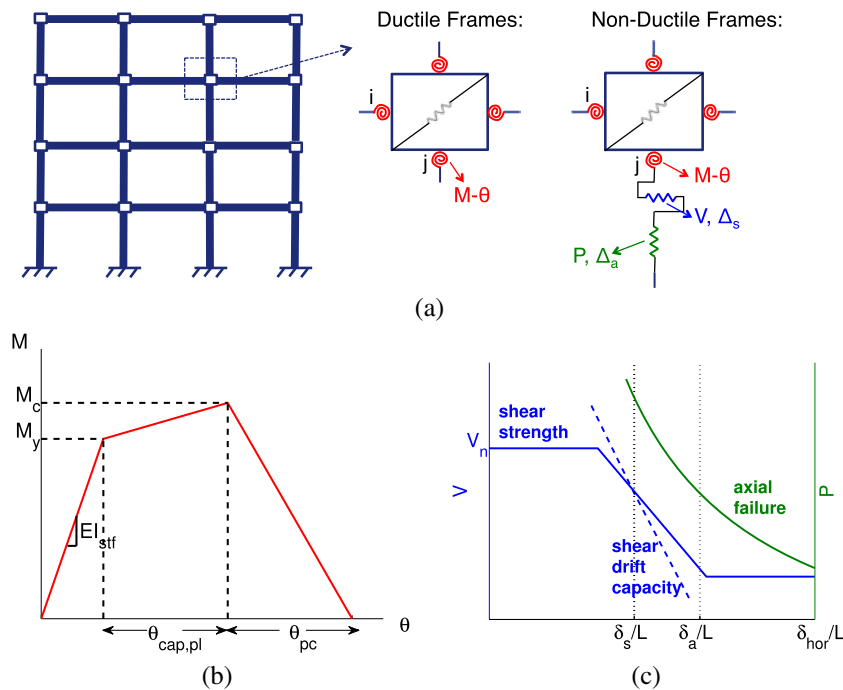
Figure 2. (a) Illustrative structural idealization of the models used in this study. Details of beam-column connections for ductile and non-ductile frames are provided. (b) Backbone curve for concentrated plasticity model (c) Illustration of the shear and axial failure models.

to characterize the behavior in the large displacement range. Detailed information about the design of buildings can be found in [29]. For both the ductile and non-ductile frames, Rayleigh damping is used with 3% equivalent critical damping in the first and third modes of the structure, and P-Δ effects are modeled using a leaning-column. The analysis models used in this study are created in two-dimensions for typical three-bay frames. By using only one frame for analysis, it is implicitly assumed that the frames in a given direction are fully correlated. This is a source of modeling uncertainty which is not addressed in this paper.

3.2. Seismic hazard analysis and ground motion selection

Each of the archetype structures are analyzed based on the seismic hazard at their corresponding design sites in Los Angeles, CA (ductile structures at 33.996°N, 118.162°W; non-ductile structures at 34.05°N, 118.25°W), where both sites have National Earthquake Hazards Reduction Program Site Class D soil. The hazard curves and deaggregation information at all sites are obtained from the United States Geological Survey (USGS) hazard curve application [33] and the 2008 USGS interactive deaggregations web tool [34], respectively. Ground motions at the five intensities, corresponding to exceedance probabilities of 5% in 50, 2% in 50, 1% in 50, 1% in 100, and 1% in 200 years, are selected using an algorithm by [2]. Suites of 200 ground motions are selected at each intensity level to provide a different motion for each structural realization that will be considered in the modeling uncertainty analyses.

3.3. Modeling uncertainty

3.3.1. Characterization of modeling uncertainty. The six parameters that define the M-θ hysteretic hinge model are treated as random variables, including the five parameters that define the backbone curve in Figure 2(b) and a sixth parameter that defines the cyclic energy dissipation capacity. Following [27], these parameters are the flexural strength (M_y), ratio of maximum moment and yield moment

capacity (M_c/M_y), effective initial stiffness which is defined by the secant stiffness to 40% of yield force ($EI_{stf,40}/EI_g$), plastic rotation capacity ($\theta_{cap,pl}$), post-capping rotation capacity (θ_{pc}), and energy dissipation capacity for cyclic stiffness and strength deterioration (γ).

For non-ductile frames, the uncertainty in the shear and axial parameters, V_n, δ_s/L, δ_a/L (Figure 2(c)) are likewise treated as random variables. These parameters were empirically calibrated and summary statistics of the predictive capacity models are reported in each respective studies [31,32]. In addition to reporting the variability in the parameters, these studies also report small biases in the model parameters (measured to calculated values of 1.05 for V_n and 0.97 for δ_s/L, δ_a/L) that are incorporated in the uncertainty analyses.

In addition to the parameters defining the beam and column component models, equivalent viscous damping ratio (ξ), column footing rotational stiffness (K_f), and joint shear strength (V_j) are also treated as random. The modeling parameters are assumed to have lognormal distributions, and the variability in these parameters are represented using logarithmic standard deviations given in Table I.

In addition to variability of the modeling parameters themselves, previous studies have shown that the assumed correlation between parameters can significantly affect the calculated collapse behavior [35]. In a previous study, we use random effects regression models on a database of reinforced concrete column tests [28] to quantify the correlations of random model parameters within and between the structural components [36]. As described by [36], correlation of parameters within components (e.g., the relationship of strength to ductility, M_y to $\theta_{cap,pl}$, within a member) were determined using each of the over two hundred column tests, and the correlation of parameters between components (e.g., the relationship of parameters for beams versus columns within a building) were determined by comparing results of specimens that were constructed and tested at different labs. For the uncertainty analyses in this study, we assumed parameters between beams within a building (beam-to-beam) and parameters between columns within a building (column-to-column) to be fully correlated, the reasoning being that they have the same details and are built by the same contractor. On the other hand, parameters between beams and columns within a building (beam-to-column) and within each component model are assumed to be partially correlated. The correlation coefficients are shown in Table II, following [36], where the coefficients in the left matrix are for parameters within components (component i to i) and the right matrix is for parameters between components (component i to j). These coefficients define the correlations using logarithms of the parameters, so that the natural logarithms of the parameters follow a multivariate normal distribution. Other than the parameters for the beam and column hinges, all other parameters are assumed to be uncorrelated.

Table I. Logarithmic standard deviations of random variables.

Random variables & dispersion values													
$\theta_{cap,pl}$	0.59	$\frac{EI_{stf}}{EI_g}$	0.27	M_y	0.31	$\frac{M_c}{M_y}$	0.10	θ_{pc}	0.73	γ	0.50
ξ	0.60	K_f	0.30	V_j	0.10	V_n	0.15	δ_s/L	0.34	δ_a/L	0.26

Table II. Correlation of random variables defining backbone curve and hysteretic behavior of a concentrated plasticity model.

Component i	Component i						Component j					
	θ_{cap,pl_i}	$\frac{EI_{stf}}{EI_g}_i$	M_{y_i}	$\frac{M_c}{M_y}_i$	θ_{pc_i}	γ_i	θ_{cap,pl_j}	$\frac{EI_{stf}}{EI_g}_j$	M_{y_j}	$\frac{M_c}{M_y}_j$	θ_{pc_j}	γ_j
θ_{cap,pl_i}	1.0	0.0	0.1	0.3	0.2	0.0	0.7	0.0	0.0	0.1	0.1	0.0
$\frac{EI_{stf}}{EI_g}_i$		1.0	0.1	−0.1	0.0	0.1		0.7	0.1	−0.1	0.0	0.0
M_{y_i}			1.0	0.3	0.1	0.1			0.9	0.2	0.1	0.1
$\frac{M_c}{M_y}_i$				1.0	0.0	0.2				0.7	0.0	0.0
θ_{pc_i}		(sym.)			1.0	0.2		(sym.)			0.3	0.0
γ_i						1.0						0.4

3.3.2. Propagation of modeling uncertainty. Monte-Carlo simulation-based uncertainty propagation methods are intuitive and straightforward to implement, and aside from the computational expense are fairly scalable to problems with many random variables. These methods involve drawing random realizations of the variables from the joint probability distributions and conducting analyses with these realizations. Latin hypercube sampling is shown to be an effective sampling method for seismic response assessment [15, 16, 36]. The effectiveness of the method results from the stratification of the probability distribution. It operates by drawing random realizations of model parameters from equal probability disjoint intervals of the range of these parameters [37]. Considering the trade off of accuracy versus computational time, we ran 200 realizations of the model parameters using Latin hypercube sampling at each ground motion intensity. Stochastic optimization using simulated annealing is applied to preserve the correlation structure among the random variables, which are obtained using Latin hypercube sampling [15]. The sampled model realizations are each matched randomly with one of the 200 ground motions at each IM level. In addition, to distinguish the influence of modeling uncertainty from record-to-record variability, we re-analyze the structures using median model parameters with the same ground motions.

4. IMPACTS OF MODELING UNCERTAINTY ON COLLAPSE RESPONSE

4.1. Effect of modeling uncertainty on collapse fragility parameters

Following the approach outlined previously in Figure 1, collapse fragility curves are computed for each structure and the impacts of modeling uncertainty are investigated by comparing ratios of median collapse capacity and dispersion (θ_c, β_c) and the collapse rates (λ_c) computed using models with and without modeling uncertainty, that is, $\beta_{c,T}/\beta_{c,RTR}$. In Figure 3, the change in median collapse capacity due to modeling uncertainty is plotted with respect to the change in the dispersion for fragility curves computed for each building archetype. Different markers are used to distinguished between the ductile and nonductile frames, ductile frames with story strength irregularities, and the number of stories. The buildings with strength irregularities include 8 and 12-story ductile frames, where the first stories have lateral strengths that are 30% less than the stories above.

As observed in Figure 3(a), modeling uncertainty tends to reduce the median collapse capacity and increase the dispersion, with a maximum reduction of 20% in $\theta_{c,T}/\theta_{c,RTR}$ and increase of 10% to 70% in $\beta_{c,T}/\beta_{c,RTR}$. Interestingly, the structures with smaller change in dispersion generally exhibit more reduction in the median collapse capacity, and vice versa. Referring to the collapse fragility and deaggregation curves in Figure 1, both of these effects will each tend to increase the collapse risk. To the extent that the change in median and dispersion tend to have opposite trends, they tend to be compensating (that is, one structure's collapse risk may increase due to a large increase in β_c, whereas the others will increase due to a reduction in θ_c). Non-ductile frames and ductile frames with soft stories are observed to display more shift in median collapse capacity, compared with the other structures. This may be explained by the observation that these systems are more sensitive to weakest link type behavior.
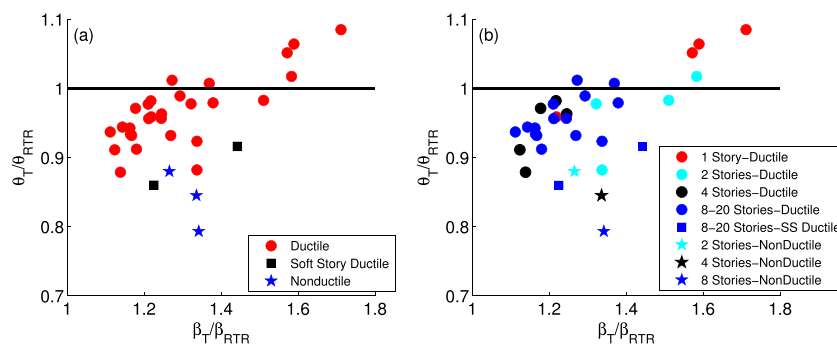

Figure 3. Change in median collapse capacity with respect to change in the dispersion values of collapse fragility curves (a) With respect to structural characteristics (b) With respect to number of stories and structural characteristics.

In Figure 3(b), the same data are grouped with respect to the number of stories and structural characteristics. Here, it is interesting to observe that the single-story buildings and a couple of the two-story buildings are the only ones to experience a large increase in dispersion, $\beta_{c,T}/\beta_{c,RTR}$, with little change in median $\theta_{c,T}/\theta_{c,RTR}$. The slight increase in median to $\theta_{c,T}/\theta_{c,RTR}$ values above 1 seems to be an artifact of the large change in dispersion that flattens out the fragility curve. These buildings tend to have only one collapse mode, such that the variability in model parameters is more directly linked to the variability in response. This is in contrast to the other buildings that generally display multiple failure modes, where the collapse mechanism can be idealized as a series of collapse mechanisms, where the weakest will generally govern. In these cases, while a particular perturbation of model parameters result in the increase of the capacity of some mechanisms, the capacity in another mechanism might decrease and can govern the response. Therefore, in general, there is a decrease in median collapse capacities for structures having more than one collapse mechanism.

4.2. *Net effect of modeling uncertainty on collapse rates*

The net effect of the change in median and dispersion due to modeling uncertainty can be quantified by integrating the resulting fragility curves with a seismic hazard curve to determine the change in mean annual frequency of collapse, λ_c. Using the hazard curves for the building sites in Los Angeles, we calculated the ratios of $\lambda_{c,T}/\lambda_{c,RTR}$ for the 33 building archetypes. The average collapse rate ratio is calculated to be about 1.8 with a coefficient of variation of 0.2, indicating that the modeling uncertainty increases the collapse risk by about 80%, relative to the risk for the median model. To further investigate how sensitive this change is to the ground motion hazard curve, we integrated the collapse fragilities with idealized hazard curves that are modeled with a power-law hazard curve of the form $\lambda = k_0 IM^{-k}$, where the hazard curve slope k is varied and k_0 is fit over the range between $Sa(T_1)$ values corresponding to 10% to 2% in 50-year exceedance probabilities (Figure 1(c)). The results of these analyses are shown in Figure 4, where each of the boxplots corresponds to the change in λ_c values for the set of archetype buildings for sites with varying hazard curve slopes. For comparison, the red boxplots (close to k equal to 3) are data from the collapse rates determined by the USGS hazard curves for the Los Angeles building sites. Lower values of k are more representative of sites in the central and eastern United States, where there are larger differences in the spectral intensities (Sa) between the 10% to 2% in 50-year exceedance probabilities.

As indicated in Figure 4, for hazard curves with smaller slopes, the modeling uncertainties tend to have a smaller effect on collapse risk, as compared with the Los Angeles site with k $\sim$ 3. Referring back to Figure 1, the reason for this relates to the relationship of the slope of the hazard curve relative to the lower tail of the collapse fragility curve. Deaggregation of λ_c helps identify the ground motion intensities that contribute most to λ_c estimates. In the presence of modeling uncertainty, the dominant
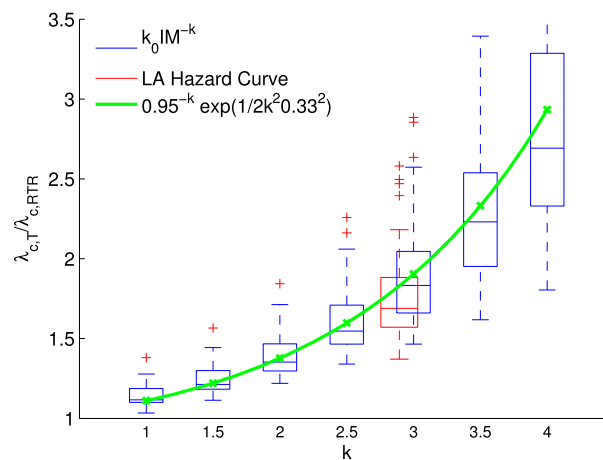

Figure 4. Change in λ_c due to modeling uncertainty.

ground motion contributors in computing λ_c is shifted toward smaller intensities (Figure 1(d)). The magnitude of the shift in dominant ground motion intensities depends on the change in fragility curve characteristics as well as the change in the instantaneous slope of the true (nonlinearized) hazard curve. The impacts of modeling uncertainty on λ_c would become more pronounced when the collapse fragility curve is pushed toward the regions of hazard curves having higher instantaneous slopes and this might result in different impacts on λ_c at different sites.

The collapse rate ratios calculated for the archetype models can be described by a closed-form expression, shown by the green curve in Figure 4. The expression for this curve is derived using a closed form expression for collapse rate λ_c by [38] as a function of median and dispersion of collapse fragility and the slope of the idealized hazard curve. Taking ratios of the rates, the change in collapse rate due to modeling uncertainty in λ_c is obtained as follows:

$$\frac{\lambda_{c,T}}{\lambda_{c,RTR}} = \left[\frac{\theta_{c,T}}{\theta_{c,RTR}}\right]^{-k} e^{\frac{1}{2}k^2 \beta_{c,M}^2} \tag{2}$$

where $\beta_{c,M}$ represents the additional dispersion due to modeling uncertainty and the other terms are as defined previously. Assuming that the modeling and record-to-record effects are statistically independent, the modeling dispersion $\beta_{c,M}$ can be estimated using a square root of sum of squares (SRSS) approach through the equation given thereafter:

$$\beta_{c,T} = \sqrt{\beta_{c,RTR}^2 + \beta_{c,M}^2} \tag{3}$$

As shown in Figure 4, the predictions by Equation (2) give good agreement using the average values from the building archetype studies, where the average median shift is 0.95 (with a coefficient of variation of 0.12) and the average $\beta_{c,M}$ is 0.33 (with a coefficient of variation of 0.18).

4.3. Equivalent value of modeling uncertainty

To the extent that the results from the archetype studies are representative to other framed buildings, it is useful to examine how the effects of modeling uncertainties can be generalized. This would inform, for example recent performance-based guidelines [39, 40] that incorporate judgment-based modeling uncertainty factors that are combined, using an SRSS rule, with other sources of variability. Figure 5(a) provides an illustration of how modeling uncertainty parameters can be used to approximate the calculated collapse fragility for the 12-story building archetype (ID 2067). Shown in Figure 5(a) are the collapse fragilities obtained from simulations for the median model ($P_{c,RTR}$) and for the models that include modeling uncertainty ($P_{c,T}$). In between are two approximate fragility curves, one that has an adjustment to the median and dispersion and the second that has only a change to the dispersion. The curve with the median shift and added dispersion is based on the average values from the archetype study (average median shift of 0.95 and average modeling uncertainty of 0.33). The other curve includes an equivalent value of modeling uncertainty of $\beta_{c,M}^*$ equal to 0.4, which is calibrated so as to match, on average, the collapse rates that are determined using the simulated collapse fragility curves ($P_{c,T}$) and the hazard curves for the archetype building studies.

The approach to calibrate the equivalent modeling uncertainty $\beta_{c,M}^*$ is as follows: (i) determine the $\lambda_{c,T}$ for each archetype collapse study; (ii) develop fragility functions for each archetype that are obtained using median model parameters for that archetype, i.e $\theta_{c,RTR}$ and $\beta_{c,RTR}$, along with an estimate of $\beta_{c,M}^*$ that is combined with $\beta_{c,RTR}$ for each archetype using the SRSS approach; (iii) integrate the estimated collapse fragility curve with the hazard curve to find an estimate of $\lambda_{c,T}$ for each archetype; and (iv) repeat steps 2 and 3, selecting updated estimates of $\beta_{c,M}^*$ to minimize the error between the correct and estimated values of $\lambda_{c,T}$, until the desired accuracy is achieved. When run for the archetype buildings reported earlier, the resulting mean value of $\beta_{c,M}^*$ is 0.4. The
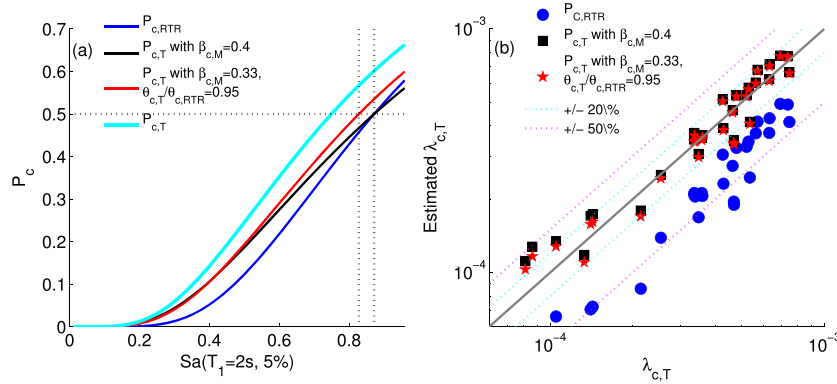
Figure 5. (a) Illustration of practical approaches to incorporate modeling uncertainty using 12-story structure with ID 2067 (b) Estimated λ_c using the practical approaches.

resulting estimates of $\lambda_{c,T}$ that are obtained using an SRSS rule with $\beta_{c,M}^*$ of 0.4 versus target values are given in Figure 5(b) using black squares. With this approach, mean measured to computed $\lambda_{c,T}$ is obtained as 1.03 with a coefficient of variation of 0.18. Also shown in Figure 5(b) are (i) red points determined based on estimated fragility curves that employ the average median shift of 0.95 and modeling dispersion of 0.33 and (ii) blue points from the median model fragility curves $\lambda_{c,RTR}$. This latter case corresponds to neglecting modeling uncertainty and leads to a significant (on average 58%) underestimation of λ_c.

From Figure 5(b), the two approximate fragility curves are shown to provide similar estimations of $\lambda_{c,T}$. This is in spite of the apparent differences in the curves shown in Figure 5(a) and occurs because the two methods yield similar estimates in the lower tail region of the collapse fragility function, which dominates the contribution to λ_c. The approximate model with the median shift and modeling dispersion approach provides a slightly better alternative compared with the sole use of $\beta_{c,M}^*$ alone, but overall, both give estimates with minimal bias (less than 3% bias) in $\lambda_{c,T}$ with a coefficient of variation close to the value of 0.18 in the original simulated results.

5. IMPACTS OF MODELING UNCERTAINTY ON DRIFT DEMANDS

In this section, impact of modeling uncertainty on drift demands is examined, first, considering drift exceedance (fragility) curves, and then evaluating the drift demands at specified intensity levels.

5.1. Influence of modeling uncertainty on drift exceedance fragility curves

Referring back again to Figure 1(b), the drift-exceedance fragility curves are quantified in a similar manner to collapse fragilities, except that the limit state is defined based on the SDR exceeding a specified sdr value, that is, $SDR \geq sdr$. Shown in Figure 6(a) are drift-exceedance fragility curves for one of the 8-story archetypes (ID 1012), plotted for results from the median model (dashed lines, representing RTR uncertainties) and for the simulations that include modeling uncertainties (solid lines, representing the total uncertainties). Drift fragilities are shown for five sdr values, ranging between 0.03 to 0.10. Note that the drift fragility for sdr equal to 0.10 is identical to the collapse fragility curve. Figure 6(b) shows the change because of modeling uncertainty in the medians ($\theta_{SDR>sdr,T}/\theta_{SDR>sdr,RTR}$) and the dispersions ($\beta_{SDR>sdr,T}/\beta_{SDR>sdr,RTR}$) of the drift fragility curves $P_{SDR>sdr}$, similar to the collapse fragility curve ratios shown previously in Figure 3. The average changes for the 33 archetypes are shown by squares, and the lines around the squares extend to 16% and 84% fractals of the change in the corresponding parameters. Figure 6(c) shows the distributions of dispersion because of modeling uncertainty as a function of sdr. In Figure 6(d), the change in mean annual exceedence rates ($\lambda_{SDR>sdr,T}/\lambda_{SDR>sdr,RTR}$) are shown, obtained from integrating the drift fragility curves with the ground motion hazard for the building site in Los Angeles.
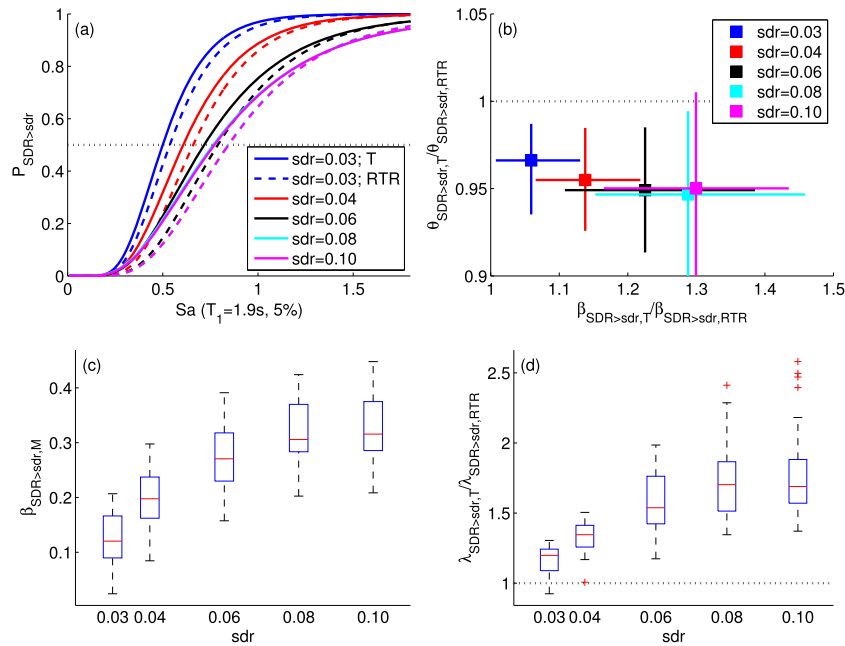
Figure 6. (a) Example drift-exceedance fragility curves for an 8-story structure with ID 1012 (b) Change in median collapse capacity with respect to change in the dispersion values of fragility curves defining drift-exceedance limit states (c) Dispersion due to modeling uncertainty as a function of story drift ratio (SDR) (d) Boxplots showing the change in $\lambda_{SDR>sdr}$ as a function of SDR.

Based on the results shown in Figure 6, for story drift ratios below 0.03, modeling uncertainties have a relatively small but measurable impact on the results. For example, at the 0.03 drift limit, modeling uncertainties increase the mean annual frequency of exceedence about on average by 20%. Compared with the reliability of nonlinear analyses, which are usually run with 10 or fewer ground motions, the influence of uncertainties would be difficult to assess. However, as there is a measurable increase in the median drift, dispersion and annual frequency, one could envision applying a reliability factor to account for the modeling uncertainties, even at these comparatively low drift levels. At peak story drifts of 0.04 and beyond the modeling uncertainties have a greater effect and may be significant. In the limit of sdr about 0.07 to 0.10, the modeling uncertainty is on roughly the same order as the uncertainties in the collapse fragility, where the dispersion ratio ($\beta_{SDR>sdr,T}/\beta_{SDR>sdr,RTR}$) increase to about 1.3 and the exceedance rate ($\lambda_{SDR>sdr,T}/\lambda_{SDR>sdr,RTR}$) increases by a factor of about 1.8. Also note that the fragility functions for sdr equal to 0.08 coincide with the fragility functions for sdr equal to 0.1 (These curves are indicated with cyan and magenta, respectively). As described previously for the collapse fragility, at large drifts in excess of sdr of 0.07, the equivalent $\beta_{c,M}$ is about 0.33.

5.2. Influence of modeling uncertainty on drift demands

We next investigate the impacts of modeling uncertainty on story drift demands at different ground motion intensity levels. This evaluation of drift demands at a specified intensity is particularly relevant to the manner in which drifts are assessed in design practice. As with the collapse fragilities, ground motion intensities evaluated in this study correspond to exceedance probabilities of 5%, 2%, and 1% in 50 years, 1% in 100 years, and 1% in 200 years. The values of SDR observed at each IM are recorded for each structure, and empirical CDFs corresponding to $P_{SDR \leq sdr}$ are obtained. Figure 7(a) compares the ECDFs of drift demands obtained using a median model (dashed lines, corresponding to RTR uncertainties) and models incorporating modeling uncertainty (solid lines, corresponding to total uncertainties) for the 8-story building archetype (ID 1012).

It is observed from Figure 7(a) that the difference in deformation demands between the median model and the model incorporating modeling uncertainty is negligible for drift ratios smaller than about 0.025. At the ground motion intensity of 2% probability of exceedance in 50 years (2/50 year),
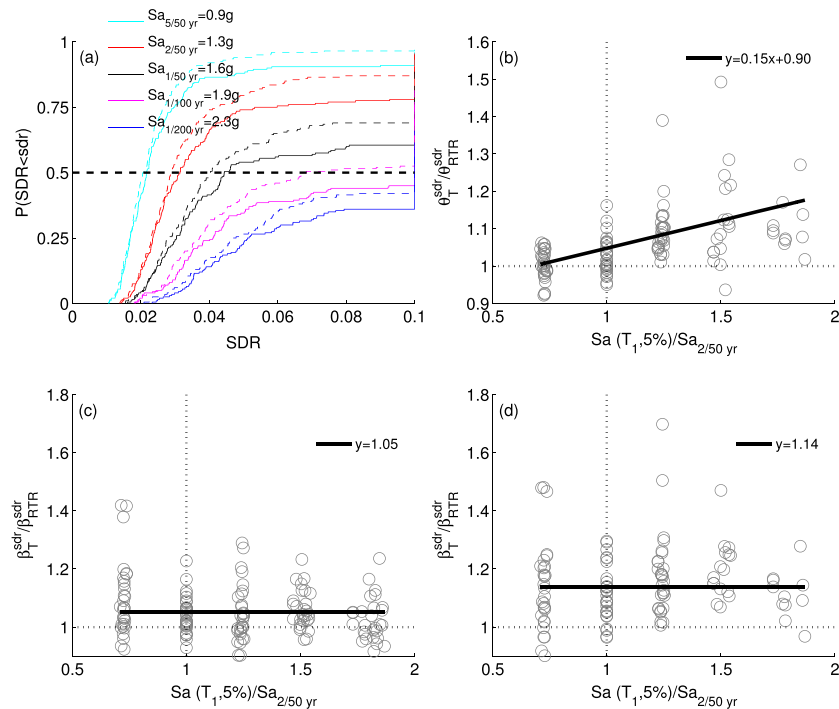
Figure 7. (a) ECDF of drift demands using median model and with modeling uncertainty for the 8-story structure with ID 1012 (b) Change in counted median of drift demand distributions w.r.t. drifts for different structures (c) Change in dispersion of the fitted lognormal distributions to sdr values of no-collapses (d) Change in dispersion of the fitted lognormal distributions to sdr values up to median.

the probability that SDR will be smaller than 0.03 is 47% using a median model, increasing to 53% in the presence of modeling uncertainty. On average for all of the building archetypes, at the 2/50 year ground motion, the probability that SDR will be smaller than 0.03 is about 4% larger in the presence of modeling uncertainty. This increases to 8% at SDR of 0.06, following the trend discussed previously of increasing impacts of modeling uncertainty with increasing drifts.

Figure 7(b) shows the change in counted medians in the presence of modeling uncertainty as a function of ground motion intensities that are normalized with respect to $Sa_{2/50 \text{ year}}$. Counted medians correspond to SDR values at the 50% probability level of Figure 7(a). For each IM level, SDR values of the solid lines divided by that of dashed lines quantify the change in counted medians of drifts. At the 5/50 year ground motion, there is no change in median drifts, but at larger intensities the ratio increases linearly, with a ratio of 1.05 at the 2/50 year intensity and up to about 1.2 at the 1/200 year intensity. For some of the building archetypes and ground motion intensity levels, more than half of the analyses results in collapse response (i.e., Figure 7(a), 1/200 year). While these collapse data points are not shown in Figure 7(b), they are incorporated in the computation of the fitted line using a maximum likelihood approach with a normal distribution by right-censoring these values at 1.

Figures 7(c) and (d) show the change because of modeling uncertainty in dispersion values of the fitted lognormal distributions to SDR values as a function of ground motion intensities that are normalized with respect to $Sa_{2/50 \text{ year}}$. Lognormal distributions are fitted to the entire set of no-collapse data in Figure 7(c), whereas, in Figure 7(d), the distributions are fit to the SDR values that are smaller than their respective medians. This latter approach was performed to better fit the lower tail of the ECDFs, because the upper portion seems to be more affected by collapse occurrences than by the non-collapse drifts.

Plots of dispersion ratios using either of the approaches (Figure 7(c) or (d)) indicate rather modest average changes of about 1.05 to 1.14 in the dispersion due to modeling. In addition, the plots do not reveal much if any trend between the change in dispersion with ground motion intensity. At first glance, this result appears to be inconsistent with the impacts observed at collapse (e.g., Figure 3); however,

the apparent difference is related to the consistent treatment of collapse and non-collapse cases, which is addressed in the following section. Overall, however, the change in dispersion of drift demands due to modeling uncertainty is practically negligible, whereas the change in median drift (Figure 7(b)) is more significant.

6. MAXIMUM CONSIDERED EARTHQUAKE LEVEL DRIFT DEMAND AND ACCEPTANCE CRITERIA

In the previous sections, we have examined the influence of modeling uncertainties on collapse risk and on drift demands, treating the two as related but distinct measures of performance. However, emerging building code design requirements that employ the use of nonlinear dynamic analysis, such as applied to tall buildings [18, 19] or in the recently proposed ASCE 7 requirements [20], rely increasingly on story drift limits to ensure building safety. Typically, these drift limits are checked under maximum considered earthquake (MCE) ground motions. In this section, we propose a framework for relating story drift demands and acceptance criteria to collapse safety goals, considering how variability due to modeling uncertainty affects these criteria.

An essential first step in establishing drift-based acceptance criteria is to determine story drift limits for collapse. This can be performed using IDA, using an approach formalized by [22]. IDA methods involve the scaling of ground motions through a range of increasing ground motion intensity levels until the structure displays dynamic instability. This enables quantification of drift capacities, which can then be related to induced story drift demands at any ground motion intensity level. An example IDA curve for one ground motion is shown by the black line in Figure 8, where the collapse capacity corresponds to the point where the curve flattens out, indicating the onset of instability.

As with MSA procedures (described previously in Figure 1), IDA procedures are usually performed with multiple ground motions to obtain statistical values of drift demands and collapse capacity. So, for example, the row of drift demands shown by the red points at the MCE intensity in Figure 8 could be one stripe of an MSA or IDA. However, an important distinction between MSA and IDA procedures is that IDA approaches usually involve scaling a single set of ground motions to larger and larger values, whereas MSA procedures use different ground motions at each intensity, which ideally are selected and scaled to match the target conditional spectra that varies with ground motion intensity. Because IDA procedures do not make this distinction, the IDA results may require adjustment of the ground motion intensities (the vertical statistics in Figure 8). This is why, for example, the Federal Emergency Management Agency (FEMA) P695 [39] procedures apply a spectral shape factor adjustment to the spectral acceleration collapse intensity. For the same reason, MSA and IDA procedures run with different record sets may have different drift demands at any ground motion intensity level. However, the IDA procedure is assumed to provide a reliable measure of the drift at collapse (using horizontal statistics in Figure 8), which is a measure that is not readily obtained using MSA procedures.
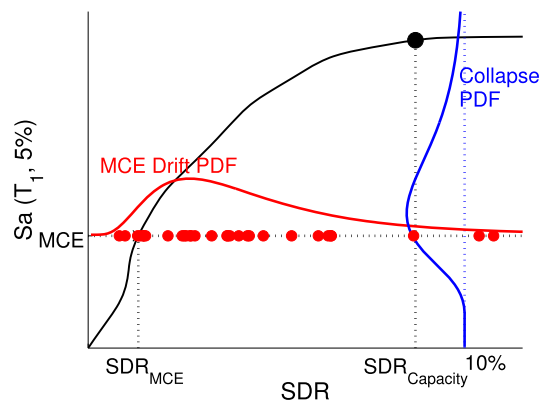

Figure 8. An example IDA curve in comparison with multiple stripe analyses data.

Ultimately, it is proposed to use IDA procedures to determine the drift at collapse, which then can be compared with the earthquake-induced drift demands determined using MSA with hazard-consistent ground motions. However, as a first step, IDA procedures will be used to characterize the joint distribution of drift demands under MCE intensity ground motions and drift capacity at the onset of collapse.

We first present the proposed framework for obtaining distributions of drift capacity and demand at MCE. Next, we apply this framework to selected archetypes and discuss the results. Finally, we examine the implication of these results on the risk-based acceptance criteria for use of nonlinear dynamic analysis in the proposed next update ASCE 7 [20].

6.1. Framework for obtaining distributions of building drift capacity and demand at MCE

Using distributions of drift capacity and demand at MCE, the probability of collapse at the MCE intensity, $P(Collapse)$, can be obtained using the equation thereafter:

$$P(Collapse) = P(D > C) \tag{4}$$

where D and C represent the distributions of drift demand at MCE and drift capacity, respectively. To evaluate Equation (4), one needs the parameters defining the joint distribution of D and C. In this study, we model the distribution of demands and capacities using a bivariate lognormal distribution, whose parameters are obtained using maximum likelihood estimation.

IDA is employed to obtain structural drift capacities and to relate these to MCE level demands. In doing so, consideration must be given to cases where collapse occurs below the MCE demand level. This is illustrated in Figure 9, which shows two example IDA curves along with the ground motion intensity corresponding to MCE. For IDA curves whose capacities are below MCE level (blue curve in Figure 9), demand at MCE can not be exactly quantified, but the available information is that demand at this level will be greater than the capacity associated with these curves. Otherwise, for IDA curves whose capacities are above MCE level (red curve in Figure 9), both the drift capacity and demand at MCE can be obtained from the associated IDA curve.

For ground motions that cause collapse below the MCE hazard level, their MCE drift demand values are capped at their drift capacity values, thus resulting in right-censored demand values. Using a maximum likelihood estimation method with right censored data, one can then determine the parameters of the joint distribution characterizing the demand at MCE and the capacity. These parameters are medians and dispersions of drift demand and drift capacity, along with the correlation between logarithms of demand and capacity, which are indicated as m_D, β_D, m_C, β_C and $\rho_{D,C}$, respectively.
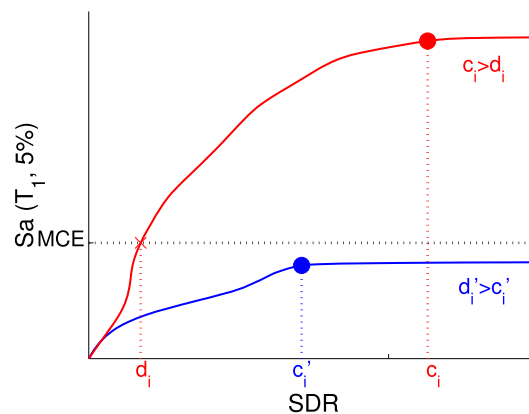

Figure 9. Two example IDA curves are provided with red and blue lines having drift capacities above and below maximum considered earthquake (MCE) level, respectively.

For IDA curves that do not exhibit collapse response at MCE ($c_i > d_i$), one can obtain the demand and capacity values directly (Figure 9). This means that demand and capacity values are not censored. The likelihood of observing $C = c_i$ and $D = d_i$ is computed using the bivariate lognormal distribution of demand and capacity:

$$Likelihood = P(C = c_i, D = d_i)$$
$$= f_{C,D}(C = c_i, D = d_i) \tag{5}$$

where $f(\cdot)$ represents a lognormal PDF.

For IDA curves that exhibit collapse response below MCE ($d_{i'} > c_{i'}$), drift demand at MCE cannot be determined, and is thus censored at its respective capacity. The likelihood of observing $C = c_{i'}$ and $D > c_{i'}$ is computed using the equation later.

$$Likelihood = P(D > c_{i'} | C = c_{i'}) f_C(c_{i'})$$
$$= \left(1 - \Phi\left(\frac{ln(c_{i'}) - ln(m_{D|C})}{\beta_{D|C}}\right)\right) f_C(c_{i'}) \tag{6}$$

where $\Phi(\cdot)$ is the standard normal CDF, and $m_{D|C}$ and $\beta_{D|C}$ are the conditional median and dispersion of demand given capacity, respectively. Because the joint distribution of demand and capacity are bivariate lognormal, the marginal PDF of capacity $f_C(c)$ has a lognormal distribution.

Assuming the observations are independent, the overall likelihood can be obtained as a multiplication of likelihood functions of individual data points:

$$Likelihood = \left(\prod_{i=1}^{m} f_{C,D}(C = c_i, D = d_i)\right) \left(\prod_{i'=1}^{n} \left(1 - \Phi\left(\frac{ln(c_{i'}) - ln(m_{D|C})}{\beta_{D|C}}\right)\right) f_C(c_{i'})\right) \tag{7}$$

where m and n refer to the total number of cases corresponding to no-collapse and collapse at MCE, respectively, and $\prod_{i=1}^{m}$ denotes a product over i values from 1 to m.

The parameters of interest can be obtained by maximizing the overall likelihood given in Equation (7) and are denoted by $\hat{m}_D, \hat{\beta}_D, \hat{m}_C, \hat{\beta}_C, \hat{\rho}_{D,C}$.

These parameters can be used with Equation (4) to estimate $P(Collapse)$ as follows:

$$\hat{P}(Collapse) = \Phi\left(-\frac{\frac{ln(\hat{m}_C)}{ln(\hat{m}_D)}}{\sqrt{\hat{\beta}_C^2 + \hat{\beta}_D^2 - 2\hat{\rho}_{D,C}\hat{\beta}_C\hat{\beta}_D}}\right) \tag{8}$$

6.2. Distributions of building drift capacity and demand at MCE for selected archetype structures

To characterize the joint distribution of demand and capacity, IDAs are conducted for selected archetype structures including modeling uncertainty. The generic FEMA P695 far-field ground motion set of [39] of 44 records is used for this purpose. Each of the records is used with an IDA approach with 4400 random structural realizations, resulting in a total of 4400 IDA curves. Drift capacity, determined from each IDA curve, is defined as the drift value corresponding to the point where the IDA curve flattens to 10% of its initial slope, beyond which drift demands tend to increase very rapidly. Note that this criteria is necessary for establishing robust horizontal statistics for drift capacity, whereas collapse ground motion intensities evaluated by vertical statistics can be determined using the less discriminating fixed drift limit of 0.10 (Figure 1).

As noted previously, the ductile reinforced concrete moment frame archetypes were designed according to 2003 IBC, using the 2002 USGS seismic design value maps. Therefore, these design value maps are used to set the intensity level for determining the MCE drift demands, which for the soil class S_d site correspond to MCE intensities of $S_{ms} = 1.5g$ and $S_{m1} = 0.9g$ [41].

Shown in Figure 10(a) are the 16%, 50% and 84% fractal IDA curves for the 12 story archetype (ID 1019), the fitted collapse fragility function as a function of $Sa(T_1)$ (vertical statistics) along with the histograms of the drift demand at MCE and the drift capacity (horizontal statistics). The joint occurrence of drift demand and drift capacity values are used to generate the scatterplot shown in Figure 10(b). The uncensored data, which corresponds to the cases that collapse above the MCE intensity, are indicated using blue dots, whereas censored data, which corresponds to cases that collapse below MCE, are indicated using red dots. The aforementioned framework equations are applied to develop the estimated probability distribution contours for drift demand and capacity shown in Figure 10(b). As indicated, this approach allows the development of a full distribution of demand versus capacity over the censored and uncensored region.

The fitted bivariate lognormal parameters of drift demands and capacities for the 12-story structure (ID 1019) and four other archetype buildings are summarized in Table III. In addition, the first row lists the MCE level ground motion intensity, $Sa(T_1)$, and the bottom two rows provide $\hat{P}(Collapse)$ computed using Equation (8) (from horizontal drift statistics) along with the $P(Collapse)$ values obtained using the collapse fragility function from IDA (vertical statistics). Ideally, the two bottom rows will agree, given that the drift demands, drift capacities, and collapse $Sa(T_1)$ values are all based on the same set of ground motions.

Based on comparisons of the calculated collapse probabilities, $P(Collapse)$, in the bottom rows of Table III, the proposed approach is validated to characterize collapse using story drift criteria. The estimated $\hat{P}(Collapse)$ value from drift distributions and target $P(Collapse)$ value from ground motion intensity capacities are fairly close. Other significant observations from the data are
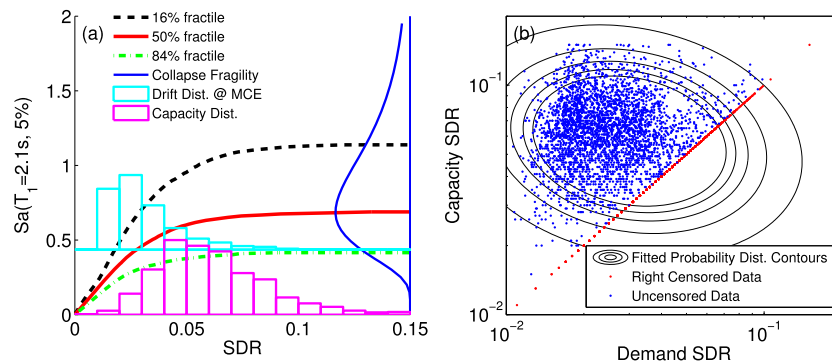

Figure 10. (a) IDA curves and drift demand at MCE and capacity histograms for ID:1019 along with collapse fragility curve (b) Probability distribution of demand at maximum considered earthquake (MCE) and capacity for ID:1019

Table III. Parameters of the joint distribution of demand and capacity and the estimated $\hat{P}(Collapse)$ along with target $P(Collapse)$ that is obtained using IDA results.

	4 Story ID: 1008	8 Story: ID 2065	12 Story: ID 1019	20 Story: ID 1021
MCE (g)	0.95	0.56	0.44	0.35
$\hat{m}_D$	0.030	0.034	0.030	0.028
$\hat{\beta}_D$	0.44	0.57	0.52	0.62
$\hat{m}_C$	0.061	0.061	0.057	0.052
$\hat{\beta}_C$	0.46	0.41	0.39	0.44
$\hat{\rho}_{D,C}$	−0.11	−0.24	−0.18	−0.04
$\hat{P}(Collapse)$	0.14	0.22	0.18	0.22
$P(Collapse)$	0.13	0.22	0.18	0.19

MCE, maximum considered earthquake.

- The median demands at MCE are about 0.03 with dispersion values ranging between 0.44 to 0.62, both of which are in line with expectations based on design level drift limits in building codes and results of other dynamic analysis studies
- The median drift capacities range from about 0.05 to 0.06 with dispersions of about 0.40 to 0.45. The median drift capacities tend to coincide with when beam and column plastic hinges tend to reach their peak point.
- The drift demands and capacities tend to be negatively correlated, where the correlation coefficients range from −00.04 to −0.24 with an average value of −0.14. This implies that in a given simulation, if the drift demand is larger than average, then the drift capacity will tend to be less than average. This is plausible from the standpoint that weaknesses (lower stiffness and strength) that tend to produce larger drifts in a given realization will likewise tend to reduce the drift at the onset of collapse. The SAC/FEMA guidelines [5] also noted the tendency for negative correlations between drift demands and capacities, and they adopt a perfect negative correlation for their computations. Drift demands and capacities are also discussed by [42, 43] to be negatively correlated, and the assumption of uncorrelated demand and capacity will result in underestimation of $P(Collapse)$.

6.3. Impacts of modeling uncertainty on the distributions of building drift capacity and demand at MCE

To evaluate the contribution of modeling uncertainty on the distributions of drift demands and capacities, we repeated the analyses just described, except using only median model parameters. This is similar to how the modeling effects were distinguished previously, except in this case the RTR variability is associated the generic FEMA P695 ground motions [39] that are used with an IDA approach. In Figure 11, the 16%, 50% and 84% fractal IDA curves and other collapse and drift distributions are shown for the 4 story archetype (ID 1008) without (Figure 11(a)) and with modeling uncertainties (Figure 11(b)). Comparing the two reveals that the modeling uncertainty significantly increases the variability in the drift capacity (magenta colored histogram) but otherwise results in relatively small changes to the other demands and capacities.

The change in the fitted bivariate lognormal parameters due to modeling uncertainty for the four building archetypes are shown in Table IV. As observed in Figure 11, the dispersion of drift capacity increases significantly, ranging from 36% to 84% with an average of 65%. In addition, the median drift capacity decreases by 5% to 9%. The MCE level median drift demand increases by about 3% to 8%, which parallels the trend noted in the counted median demands using MSA (Figure 7(b)). The reverse trends in median drift capacity and drift demands also follows from the negative correlations noted previously. The change in dispersion of MCE drift demands ranges from -6% to 5%, which is almost insignificant and consistent with the results shown previously using MSA (Figures 7(c) and (d).

In summary, the major effects of modeling uncertainty are to (1) significantly increase the dispersion in the drift capacity by about 65%, and (2) reduce the margin between the median drift demands and capacities by about 12%.
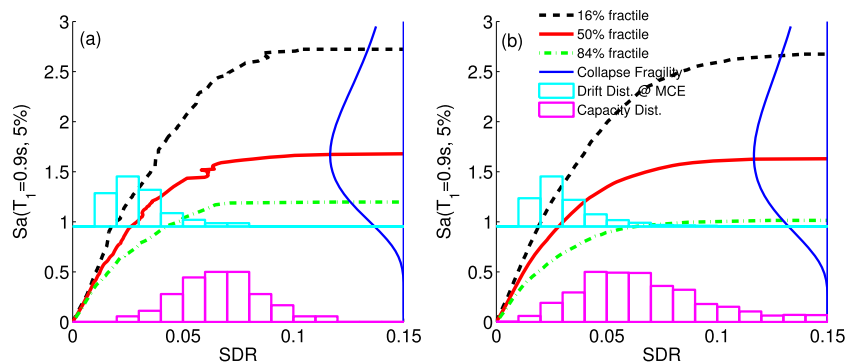

Figure 11. IDA curves and drift demand and capacity histograms in terms of drifts for ID:1008 (a) using median model (b) with modeling uncertainty.

Table IV. Change in the parameters of the joint distribution of demand and capacity due to modeling uncertainty.

	4 Story ID: 1008	8 Story: ID 2065	12 Story: ID 1019	20 Story: ID 1021
$\hat{m}_{D,T}/\hat{m}_{D,RTR}$	1.05	1.04	1.08	1.03
$\hat{\beta}_{D,T}/\hat{\beta}_{D,RTR}$	1.05	0.99	1.03	0.94
$\hat{m}_{C,T}/\hat{m}_{C,RTR}$	0.95	0.91	0.93	0.94
$\hat{\beta}_{C,T}/\hat{\beta}_{C,RTR}$	1.59	1.84	1.36	1.80

Table V. Probability of collapse and mean and median drift demand at MCE obtained using generic and hazard consistent ground motions.

		4 Story ID: 1008	8 Story:ID 2065	12 Story:ID 1019	20 Story:ID 1021
Generic GMs	m_D	0.030	0.034	0.030	0.028
	μ_D	0.033	0.040	0.034	0.034
	$\hat{P}(Collapse)$	0.14	0.22	0.18	0.22
	$P(Collapse)$	0.13	0.22	0.18	0.19
Hazard Consistent GMs	m_D	0.026	0.029	0.024	0.020
	μ_D	0.029	0.034	0.027	0.024
	$\hat{P}(Collapse)$	0.13	0.16	0.14	0.17
	$P(Collapse)$	0.10	0.18	0.13	0.16

6.4. Evaluation of ASCE 7 story drift acceptance criteria – building archetype results

The ASCE 7 provisions [20] indicate that for typical (risk category 1&2) buildings the probability of collapse at MCE should be less than 10%. The provisions further formalize these risk targets to limit the probabilities of collapse to 10%, 6%, and 3% under MCE intensities for buildings in risk categories 1&2, 3, and 4, respectively. Presumably, the design acceptance criteria should be based on these collapse safety targets; however, in explaining the newly proposed provisions for design verification by nonlinear dynamic analysis the authors [44] note that the specified MCE drift limits are based primarily on calibration to existing story drift limits, which were established long before formal risk targets were proposed. With the aim toward providing a sounder basis for the drift limits in ASCE 7 [20] and similar standards, these limits are evaluated through the probabilistic framework proposed in this paper for relating earthquake drift demands to collapse capacities.

The archetype buildings described previously are considered to represent buildings in risk category 1&2, for which the proposed new requirements in ASCE 7 [20] for design acceptance by nonlinear dynamic analysis stipulate a story drift ratio limit of 0.05 for buildings of 4 or less stories and 0.04 for taller buildings. The limit is to be compared with the average of the peak story drift demands when the building subjected to eleven pairs of ground motions that are scaled to the MCE intensity.

In Table V, the mean and median MCE drift demands (m_D and μ_D) are reported for four archetype buildings along with the computed probability of collapse, $\hat{P}(collapse)$, which is determined using the collapse assessment framework. Values of $P(Collapse)$ are also reported, which are obtained using the collapse fragility functions of the respective structure from the IDA. Because the drift demands and resulting collapse probabilities from the IDA are based on ground motions whose spectral shapes may not be consistent with the actual hazard, we also provide in Table III the median MCE drift demands and $P(Collapse)$ using hazard consistent ground motions from the MSA procedure. We similarly computed and report in Table III the resulting $\hat{P}(collapse)$ and mean drift demand (μ_D) using the hazard consistent MCE median drift demands along with the other parameters of demand and capacity that are given in Table III for each structure.

For the 4-story archetype (ID:1008), the mean demand from the risk consistent MSA motions is 0.029, which is considerably less than the ASCE 7 MCE drift limit of 0.05. Thus, this would imply that the building meets the ASCE 7 safety criterion by a considerable margin. Yet, the $P(Collapse)$

is calculated as 10% (bottom row of table) which is exactly equal to the maximum collapse risk target in ASCE 7. The approximate procedure based on relating drift demands to capacity would give $\hat{P}(collapse)$ equal to 13%. Thus, one can imagine that if the building were less stiff or strong, such that it just met the 0.05 drift limit that the structure would not meet the safety requirement. For comparison, although not directly relevant to this argument, the MCE drift demand (0.033) and probabilities of collapse (0.13 and 0.14) from the IDA procedure are slightly higher than those of the hazard consistent MSA procedure.

Similar results to the 4-story archetype are reported in Table III for the 8-story, 12-story, and 20-story archetypes, all of which meet by a reasonable margin the ASCE 7 MCE drift limit of 0.04 drift (with μ_D values for the MSA ground motions of 0.034, 0.027, and 0.024). However, all of the buildings fail to meet the maximum collapse probability limit of 10% at MCE. As indicated in the bottom row of the table, the calculated $P(Collapse)$ values range from 13% to 18%.

It should be noted that similar nonlinear analysis requirements for tall buildings [18, 19] specify more stringent MCE drift limits of 0.03, as compared with the values of 0.04 to 0.05 in ASCE 7. In looking at the drift demands and collapse probabilities for the four building archetypes in Table III, the 0.03 drift limit would appear to be more consistent with the target collapse probability limit of 10% at MCE.

6.5. Evaluation of ASCE 7 story drift acceptance criteria – parametric analysis

To further investigate the proposed ASCE 7 Chapter 16 drift requirements, we used the dispersions in the drift demands and drift capacities from the building archetype studies to parametrically evaluate the relationship between the drift limits and the implied collapse probabilities. Based on the data shown previously in Table III, the dispersions in MCE drift demand and drift collapse capacity, β_D and β_C, are assumed equal to 0.55 and 0.45, respectively. Using these values, the ratio of median (and mean) drift demands and capacities can be related to the probability of collapse using Equation (8).

As a first exercise, using the specified drift limits and target probabilities from ASCE 7 Chapter 16 [20], the implied drift capacities can be back-calculated. For buildings in risk categories 1&2, 3, and 4, the specified drift limits are 0.04, 0.03, and 0.02, and the target probabilities of collapse are 10%, 6%, and 3%. Using the assumed dispersions with no correlation between drift demand and capacities, the resulting probability distributions are determined and plotted in the left column of Figure 12. From these, the implied mean story drift capacities are 0.095, 0.086, and 0.072, for risk risk categories 1&2, 3, and 4, respectively. A few observations of these values: (i) the values are all larger than the collapse mean drift ratios of 0.057 to 0.068 (obtained from the median drift capacities in Table III), and (ii) it is counter intuitive that the drift capacities would be smaller for the higher risk categories, suggesting that there is a relative inconsistency between the drift limits and failure probabilities for the different risk categories.

As a second exercise, constant values of drift capacities will be assumed for buildings in all three risk categories, and allowable drift limits will then be calculated. For this analysis, the mean drift capacities are assumed to range between 0.06 and 0.10, where the 0.06 estimate is based on the results of our archetype study and the 0.10 is an upper bound estimate. Similar values are assumed for dispersions with a correlation between drift demand and capacities of −0.15, which is based on the data shown previously in Table III. Shown in the right side of Figure 12 are probability distributions for capacity and the corresponding drift limits assuming an intermediate collapse drift capacity of 0.08. In this case, the allowable drift limits would be 0.032, 0.026, and 0.020 for risk categories 1&2, 3, and 4, respectively. Interestingly, the calculated drift limit of 0.032 for risk categories 1&2 is close to the limit of 0.03 specified in the tall building guidelines [18], and the calculated drift limit of 0.02 for risk category 4 is equal to the current limit specified in ASCE 7 [20]. These values, along with the calculated drift limits corresponding to drift capacities of 0.06 and 0.10 are summarized in Table VI. Comparing these with current standards suggest that the current ASCE 7 drift limits would meet the target collapse risk if the story drift capacity is 0.10. However, to the extent that the upper bound drift capacity of 0.10 may be too optimistic (and well in excess of the values of 0.06 calculated in the building archetype study), this would suggest that the ASCE 7 drift limits should be reduced.
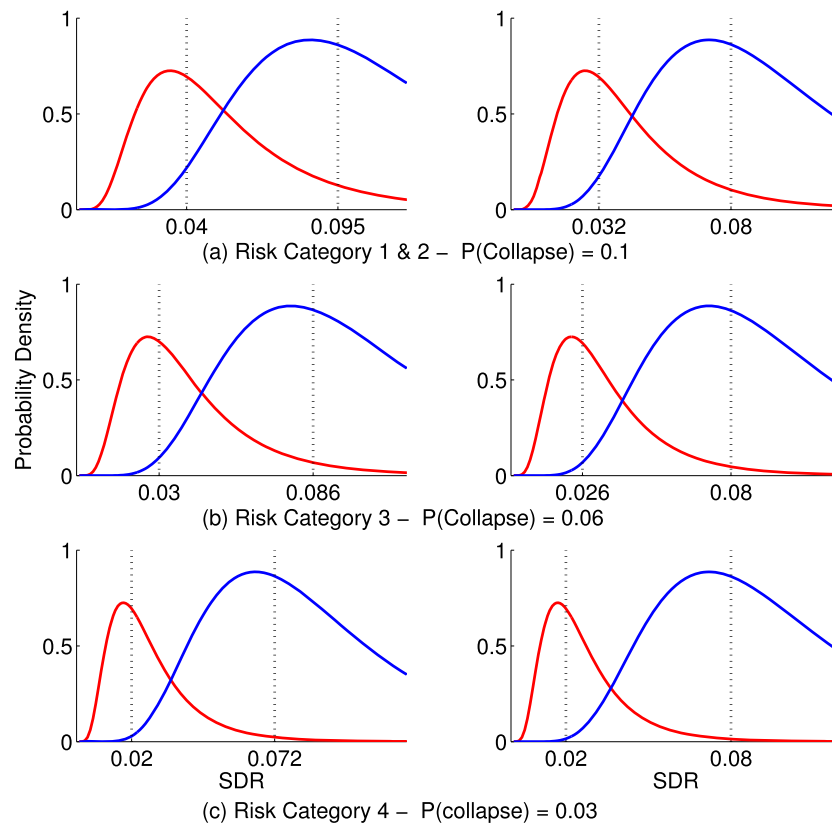
Figure 12. Back-calculated (left) and proposed (right) distributions of drift demands and capacities for buildings having more than 4 stories (a) Risk categories 1 and 2 (b) Risk category 3, and (c) Risk category 4. Red and blue lines represent the distributions of demand and capacity, respectively. Mean values are indicated with dashed black lines.

Table VI. Story drift limits for global acceptance criteria corresponding to drift capacities of 0.06 to 0.10.

μ_C	Risk categories		
	1 & 2	3	4
0.06	0.024	0.019	0.015
0.08	0.032	0.026	0.020
0.10	0.04	0.032	0.025

7. CONCLUSIONS

In this study, we characterize and propagate modeling uncertainty and quantify its impacts on the seismic response assessment of structures. The uncertainty in parameters defining analysis models and limit state surfaces are incorporated into nonlinear dynamic analysis for ductile and non-ductile reinforced concrete frame structures. Variability and correlations in structural model parameters are propagated in the dynamic analyses using Monte-Carlo simulation with Latin hypercube sampling. Earthquake ground motions are incorporated through MSA with hazard consistent ground motions that are selected and scaled using a conditional spectra approach. Impacts of modeling uncertainty are evaluated for fragility functions and mean annual exceedance rates for drift limits and collapse as well as drift (deformation) demands and capacities of thirty-three archetype building configurations.

In analyses of the archetype concrete moment frame buildings, the modeling uncertainty both shifted the medians and increased dispersion in the collapse fragility curves. The median collapse intensity (spectral accelerations) shifted by up to −20% downward or +10% upward, with an average shift of downward of about −5%. Dispersion (variability) in the collapse fragilities increased by about 10% to 70% with an average increase of about 30%. Cases with small upward (positive) shifts in medians were usually accompanied by the largest increases in dispersion, which tends to flatten out the fragility curve. The largest downward (negative) shifts in median tend to occur in structures having weak story mechanisms and non-ductile frames, where weakest link failure mechanisms are more prevalent. When integrated with earthquake hazard curves for a high-seismic region of California, the modeling uncertainty increased the mean annual frequencies of collapse, λ_c, by about 1.4 to 2.6 times, compared with the analyses that only include ground motion record-to-record variability. Subject to the same assumptions in modeling parameters, investigation of sites with hazard curves more representative of the mid and eastern United States suggest that the influence of modeling uncertainties will be smaller for these regions.

Equivalent parameters to represent modeling uncertainties in collapse fragilities are back calculated using an SRSS approach to combine variabilities due to ground motions (record-to-record) and structural modeling and by calibration to achieve consistent mean annual frequency rates for the high-seismic site. From these analyses, the average effect of modeling uncertainty on collapse fragility can be represented by either (i) a shift in median by −5% combined with an added modeling dispersion $\beta_{c,M}$ of 0.33, or (ii) no shift in median and an added modeling dispersion of $\beta_{c,M}$ of 0.40. These general values are, of course, subject to the limitations of the study of concrete moment frames designed for a high-seismic site.

The impacts of modeling uncertainty on drift-exceedance limit states are observed to generally be smaller than for collapse and vary depending on the magnitude of the drifts (amount of inelasticity). For drift-exceedance fragility curves at drift ratios of 0.03, the modeling uncertainty resulted in a small negative shift in median and increase in dispersion, which increased the mean annual frequency of drift exceedance up to 1.3 times with an average increase of about 1.2, compared with the models with only ground motion variability. At drift-exceedance ratios of 0.07, the changes in drift-fragility curves and mean annual exceedance rates were about the same as for the changes in collapse fragilities, with increases in mean annual frequencies of 1.4 to 2.6 times with an average increase of about 1.8 times, compared with cases with only ground motion variability.

To help inform the calibration of drift limits for design using nonlinear dynamic analysis, we developed a framework for quantifying the joint probability distributions of story drift demands and story drift collapse capacities. This framework considers joint treatment of analysis causing collapses and no-collapses to develop consistent estimates of story drift collapse capacities from IDA that include both ground motion and modeling uncertainties. Applying this framework to four archetype buildings provides estimates of drift demands at MCE-level ground motion intensity and drift collapse capacities. The resulting median drift capacities range from story drift ratios of about 0.052 to 0.061, with and average dispersion of 0.45. Drift demands of the archetypes, calculated at MCE level conditional spectra intensities, range from 0.028 to 0.034, with an average dispersion of 0.55. A small negative correlation of −0.14 is obtained between drift demands and capacities. The analyses further indicate that modeling uncertainty (i) increases the median MCE drift demands by about 5%, (ii) increases the dispersion in MCE demand by a negligible amount, (iii) reduces the drift collapse capacity by about 7%, and (iv) increases the dispersion in drift collapse capacity by about 65%. Thus, the combined effects of median shifts and increased dispersion on collapse drift capacity can have a significant effect on increasing the probability of drift demands exceeding drift capacities.

Finally, the procedure and data for evaluating MCE level drift demands and drift capacities are used to assess the nonlinear analysis procedures and drift limits in a recently proposed new chapter 16 in ASCE 7 [20]. Subject to the limited scope of our study, the proposed MCE level drift limits are found to be unconservative and inconsistent with the stated acceptable collapse risk targets in ASCE 7. For example, whereas the proposed drift limits for risk category 1&2 buildings range from 0.04 to 0.05, our analyses suggest that the limits should be about 0.03, which coincidentally is the specified drift limit in tall building guidelines for design by nonlinear analysis [18, 19].

The methods and strategies employed in this paper to characterize and propagate modeling uncertainties are based on fairly well established approaches. The main challenge has been in characterizing the model parameter uncertainties, developing and verifying the nonlinear analysis models, and setting up procedures to conduct the simulations and process the output. The tools and methods presented in this paper can be used to explore the impacts of modeling for other building archetypes and performance metrics. As shown in these examples, the importance of considering modeling uncertainty depends, in part, on the particular demand parameters or performance metrics of interest. More importantly, these examples demonstrate the feasibility, through modern information and computing technologies, of rigorously propagating model uncertainty to develop more reliable and risk-consistent methods for seismic assessment and design of buildings and other structures.

REFERENCES

1. Bradley BA. A generalized conditional intensity measure approach and holistic ground-motion selection. *Earthquake Engineering & Structural Dynamics* October 2010; **39**(12):1321–1342 (en).
2. Jayaram N, Lin T, Baker JW. A computationally efficient ground-motion selection algorithm for matching a target response spectrum mean and variance. *Earthquake Spectra* 2011; **27**(3):797–815.
3. Bradley BA. A critical examination of seismic response uncertainty analysis in earthquake engineering. *Earthquake Engineering & Structural Dynamics* September 2013; **42**(11):1717–1729.
4. Terzic V, Schoettler MJ, Restrepo JI, Mahin SA. Concrete column blind prediction contest 2010: outcomes and observations. *Technical Report PEER 2015/01*, Pacific Earthquake Engineering Research Center, University of California at Berkeley: Berkeley, California, 2015.
5. Cornell C, Jalayer F, Hamburger R, Foutch D. Probabilistic Basis for 2000 SAC Federal Emergency Management Agency Steel Moment Frame Guidelines. *Journal of Structural Engineering* 2002; **128**(4):526–533.
6. Wen YK, Ellingwood BR, Veneziano D, Bracci J. Uncertainty modeling in earthquake engineering. *Technical Report Project FD-2 Report*, Mid-America earthquake center: Citeseer, 2003.
7. Kennedy RP, Ravindra MK. Seismic fragilities for nuclear power plant risk studies. *Nuclear Engineering and Design* 1984; **79**(1):47–68.
8. Wen YK, Ellingwood BR. The role of fragility assessment in consequence-based engineering. *Earthquake Spectra* 2005; **21**(3):861–877.
9. Porter KA, Beck JL, Shaikhutdinov RV. Sensitivity of building loss estimates to major uncertain variables. *Earthquake Spectra* 2002; **18**(4):719–743.
10. Ibarra LF, Krawinkler H. Global collapse of frame structures under seismic excitations. *Technical Report*, John A. Blume Earthquake Engineering Center: Stanford, CA, 2005.
11. Celik OC, Ellingwood BR. Seismic fragilities for non-ductile reinforced concrete frames Role of aleatoric and epistemic uncertainties. *Structural Safety* January 2010; **32**(1):1–12.
12. Lee TH, Mosalam KM. Seismic demand sensitivity of reinforced concrete shear-wall building using FOSM method. *Earthquake Engineering & Structural Dynamics* November 2005; **34**(14):1719–1736.
13. Haselton CB. Assessing seismic collapse safety of modern reinforced concrete moment frame buildings. *Ph.D. Thesis*, Stanford University, 2006.
14. Liel AB, Haselton CB, Deierlein GG, Baker JW. Incorporating modeling uncertainties in the assessment of seismic collapse risk of buildings. *Structural Safety* 2009; **31**(2):197–211.
15. Dolsek M. Incremental dynamic analysis with consideration of modeling uncertainties. *Earthquake Engineering & Structural Dynamics* May 2009; **38**(6):805–825.
16. Vamvatsikos D, Fragiadakis M. Incremental dynamic analysis for estimating seismic performance sensitivity and uncertainty. *Earthquake engineering & structural dynamics* 2010; **39**(2):141–163.
17. Yin YJ, Li Y. Seismic collapse risk of light-frame wood construction considering aleatoric and epistemic uncertainties. *Structural Safety* July 2010; **32**(4):250–261.
18. PEER. Guidelines for performance-based seismic design of tall buildings. *Technical Report 2010/05*, Pacific Earthquake Engineering Research Center, University of California at Berkeley: Berkeley, California, 2010. Prepared by the TBI Guidelines Working Group.

19. LATBSDC. An alternative procedure for seismic analysis and design of tall buildings located in the Los Angeles Region. *Technical Report 2014 Edition with 2015 Supplements*, Los Angeles Tall Buildings Structural Design Council: Los Angeles, 2015.

20. American Society of Civil Engineers Standards Committee. *Proposal to revise the 2010 edition of asce/sei 7*: Reston, VA, 2015.

21. Lin T, Harmsen SC, Baker JW, Luco N. Conditional spectrum computation incorporating multiple causal earthquakes and ground-motion prediction models. *Bulletin of the Seismological Society of America* 2013; **103**(2A): 1103–1116.

22. Vamvatsikos D, Cornell CA. Incremental dynamic analysis. *Earthquake Engineering & Structural Dynamics* 2002; **31**(3):491–514.

23. Eads L, Miranda E, Krawinkler H, Lignos DG. An efficient method for estimating the collapse risk of structures in seismic regions. *Earthquake Engineering & Structural Dynamics* 2012; **42**:25–41 (en).

24. IBC. *International building code*. International Code Council (ISBN: 189239797), 2003.

25. American Society of Civil Engineers. *ASCE standard 7-02: Minimum design loads for buildings and other structures*: Reston, VA, 2002.

26. McKenna F, Fenves GL, Scott MH, Jeremic B. Open system for earthquake engineering simulation, 2014. Pacific Earthquake Engineering Research Center, Berkeley, CA.

27. Ibarra LF, Medina RA, Krawinkler H. Hysteretic models that incorporate strength and stiffness deterioration. *Earthquake Engineering & Structural Dynamics* October 2005; **34**(12):1489–1511.

28. Haselton CB, Liel AB, Lange ST, Deierlein GG. Beam-column element model calibrated for predicting flexural response leading to global collapse of RC frame buildings. *Technical Report PEER 2007/03*, Pacific Earthquake Engineering Research Center, University of California at Berkeley: Berkeley, California, 2008.

29. Raghunandan M, Liel AB, Luco N. Collapse risk of buildings in the pacific northwest region due to subduction earthquakes. *Earthquake Spectra* 2015; **31**(4):2087–2115.

30. UBC. Uniform building code, *International Conference of Building Officials*: Whittier: Pasadena, California, 1967.

31. Elwood KJ. Modelling failures in existing reinforced concrete columns. *Canadian Journal of Civil Engineering* October 2004; **31**(5):846–859.

32. Sezen H. Seismic behavior and modeling of reinforced concrete building columns. *Ph.D. Thesis*, Civil and Environmental Engineering, University of California, Berkeley, 2002.

33. USGS Hazard curve application. (Available from: http://geohazards.usgs.gov/hazardtool/application.php.) [Accessed: 2015-08-09].

34. USGS 2008 interactive deaggregations. (Available from: http://geohazards.usgs.gov/deaggint/2008/.) [Accessed: 2015-08-09].

35. Haselton C, Mitrani-Reiser J, Goulet C, Deierlein GG, Beck JL, Porter KA, Stewart J, Taciroglu E. An assessment to benchmark the seismic performance of a code-conforming reinforced-concrete moment-frame building. *Technical Report 2007/12*, Pacific Earthquake Engineering Research Center, University of California at Berkeley: Berkeley, California, 2007.

36. Ugurhan B, Baker JW, Deierlein GG. Uncertainty estimation in seismic collapse assessment of modern reinforced concrete moment frame building, *Proceedings of the 10th National Conference in Earthquake Engineering*. Earthquake Engineering Research Institute: Anchorage, AK, 2014.

37. Helton JC, Davis FJ. Latin hypercube sampling and the propagation of uncertainty in analyses of complex systems. *Reliability Engineering & System Safety* 2003; **81**(1):23–69.

38. Jalayer F. Direct Probabilistic seismic anaysis: implementing non-linear dynamic assessments. *Ph.D. Thesis*, Stanford University, 2003.

39. FEMA. *Quantification of Building Seismic Performance Factors*, FEMA-P695, Federal Emergency Management Agency: Washington DC, 2009.

40. FEMA. *Seismic Performance Assessment of Buildings*, FEMA-P58, Federal Emergency Management Agency: Washington, DC, 2012.

41. Haselton CB, Baker JW, Liel AB, Deierlein GG. Accounting for ground-motion spectral shape characteristics in structural collapse assessment through an adjustment for epsilon. *Journal of Structural Engineering* 2009; **137**: 332–344.

42. Kazantzi AK, Vamvatsikos D, Lignos DG. Seismic performance of a steel moment-resisting frame subject to strength and ductility uncertainty. *Engineering Structures* November 2014; **78**:69–77.

43. Jalayer F, Franchin P, Pinto PE. A scalar damage measure for seismic reliability analysis of RC frames. *Earthquake Engineering & Structural Dynamics* October 2007; **36**(13):2059–2079 (en).

44. Haselton CB, Fry A, Baker JW, Hamburger RO, Whittaker AS, Stewart JP, Elwood KJ, Luco N, Hooper JD, Charney FA, Zimmerman RB, Pekelnicky RG. Response-history analysis for the design of new buildings: a fully revised chapter 16 methodology proposed for the 2015 NEHRP Provisions and the ASCE/SEI 7-16 Standard, *Proceedings of the 10th National Conference in Earthquake Engineering*. Earthquake Engineering Research Institute: Anchorage, AK, 2014.